Large negative magnetoresistance in antiferromagnetic Gd_2Se_3

Santosh Karki Chhetri,[1] Gokul Acharya,[1] David Graf,[2] Rabindra Basnet,[1,3] Sumaya Rahman,[4] M. M. Sharma,[1] Dinesh Upreti,[1] Md Rafique Un Nabi,[1,6] Serhii Kryvyi,[4] Josh Sakon,[5] Mansour Mortazavi,[3] Bo Da,[7] Hugh Churchill,[1,4,6] and Jin Hu[1,4,6,8,*]

[1]*Department of Physics, University of Arkansas, Fayetteville, Arkansas 72701, USA*
[2]*National High Magnetic Field Lab, Tallahassee, Florida 32310, USA*
[3]*Department of Chemistry & Physics, University of Arkansas at Pine Bluff, Pine Bluff, Arkansas 71603, USA*
[4]*Material Science and Engineering Program, Institute for Nanoscience and Engineering, University of Arkansas, Fayetteville, Arkansas 72701, USA*
[5]*Department of Chemistry & Biochemistry, University of Arkansas, Fayetteville, Arkansas 72701, USA*
[6]*MonArk NSF Quantum Foundry, University of Arkansas, Fayetteville, Arkansas, USA*
[7]*Center for Basic Research on Materials, National Institute for Materials Science, Tsukuba, Ibaraki 305-0044, Japan*
[8]*Smart Ferroic Materials Center, University of Arkansas, Fayetteville, Arkansas 72701, USA*

(Received 19 July 2024; revised 20 September 2024; accepted 2 January 2025; published 22 January 2025)

Rare earth chalcogenides provide a great platform to study exotic quantum phenomena such as superconductivity and charge density waves. Among various interesting properties, the coupling between magnetism and electronic transport has attracted significant attention. Here, we report the investigation of such coupling in α-Gd_2Se_3 single crystals through magnetic, calorimetric, and transport property measurements. α-Gd_2Se_3 is found to display an antiferromagnetic ground state below 11 K with metamagnetic spin-flop transitions. The magnetic fluctuations remain strong above the transition temperature. Transport measurements reveal an overall metallic transport behavior with a large negative magnetoresistance of approximately 65% near the magnetic transition temperature, together with positive magnetoresistance near the field-induced spin-flop transitions, which can be understood in terms of the suppression of spin scattering by the magnetic field.

DOI: 10.1103/PhysRevB.111.014431

I. INTRODUCTION

Rare-earth chalcogenides display a variety of stoichiometric compositions such as RX, RX_2, RX_3, R_3X_4, and R_2X_3, where R represents rare earth, and X represents chalcogen S, Se, and Te [1]. Rare-earth chalcogenides have attracted significant interest because of their unique electronic, magnetic, optical, thermoelectric, and topological properties [2–9], which arise from or are related to the $4f$ electrons of rare earth [10,11]. In addition, tunable band gap, strong photoluminescence, and efficient luminescent properties make them promising candidates for next-generation lighting and display technologies [12–14].

Rare-earth monochalcogenide RX crystallizes in a NaCl-type structure [15,16]. Under high pressure, RX undergoes a structural phase transition to a CsCl-type [17–21], which is accompanied by a transition from semiconducting-like to metal-like transport properties. It has been predicted that when reducing the dimensionality to the two-dimensional limit, i.e., a single atomic layer, some rare-earth monochalcogenides such as TmX and YbX possess a honeycomb hexagonal lattice and display piezoelectricity [22]. In addition, for other group-III monochalcogenides ScX and YX, their single layer has also been predicted to distort to a wrinkled structure, which can lead to Dirac points and nodal lines near the Fermi level [23].

Rare-earth di- and tri-chalcogenides RX_2 and RX_3 possess layered structures formed from the stacking of chalcogen X and rare-earth-chalcogen R-X layers. In RX_2, the structure is characterized by alternative stacking of single X and single R-X layers, while the stacking of double X and single R-X layers forms RX_3 [5]. Interestingly, the lattice is tunable by vacancies in the chalcogen layers. Despite an overall layered structure, various tetragonal, orthorhombic, triclinic, and monoclinic structural variations have been reported [24–26]. Among various RX_2 and RX_3, the telluride compounds have been studied extensively because of their $4f$ magnetism [25,27,28] and diverse properties such as large negative magnetoresistance [29], charge density waves [30–34], and pressure- or doping-induced superconductivity [34–39].

Compared to mono-, di-, and trichalcogenides, sesquichalcogenides R_2X_3 are less explored. The reported studies are mainly focused on sulfides R_2S_3, for which diverse crystal structures such as orthorhombic, tetragonal, cubic, monoclinic, and rhombohedral (usually denoted by α, β, γ, δ, and ε, respectively) have been identified [40–49]. Many orthorhombic α-R_2S_3 have been reported to show single or multiple antiferromagnetic (AFM) transitions [50–54], except for α-Sm_2S_3, which shows weak ferromagnetism at low temperatures [55]. For sesqui-selenides, the earlier studies were mainly focused on crystal structures [56,57], thermoelectric, and optical properties [3,9]. For tellurides R_2Te_3, in addition to the thermoelectric properties [9], recent work has revealed an AFM semimetal state in orthorhombic α-Gd_2Te_3 [58].

*Contact author: jinhu@uark.edu

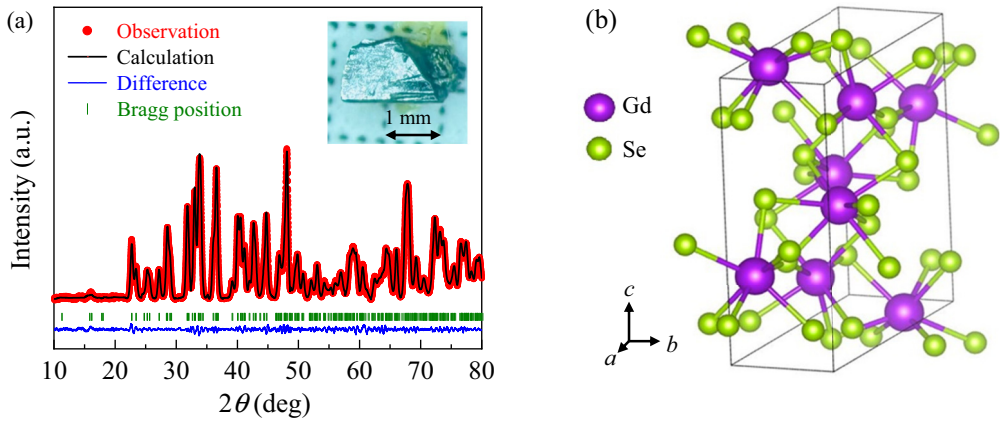

FIG. 1. (a) Powder XRD data and the Rietveld refinement of α-Gd_2Se_3. Inset shows image of a α-Gd_2Se_3 single crystal. (b) Crystal structure of the orthorhombic α-Gd_2Se_3 obtained from the refinement. The structure parameters are provided in Table I.

In this work, we extend the study to Gd_2Se_3 owing to the possible strong magnetism from the half-filled f-orbital of Gd^{3+}, which may interplay with other degrees of freedom and give rise to exotic properties such as the gigantic isotropic magnetoresistance and insulator-to-metal transition [59]. The cubic Gd_2Se_3 crystallizing in a defect Th_3P_4-type structure (due to Gd vacancies) has been reported to be a semiconductor [9,60,61]. To explore the interaction between magnetism and electronic transport, we switch to a different structure type, i.e., the orthorhombic α phase, because previous studies revealed a semiconductor state in α-Gd_2S_3 [50], but the semimetal phase in α-Gd_2Te_3 [58]. Indeed, we report an AFM ground state and metallic transport properties in α-Gd_2Se_3. More interestingly, this material displays a large negative magnetoresistance, which evinces strong coupling between magnetism and transport and is attributed to the suppression of strong spin scattering under a magnetic field.

II. EXPERIMENT

The Gd_2Se_3 single crystals used in this work were prepared by a two-step chemical vapor transport (CVT) method. First, the precursor for CVT was prepared by heating the mixture of Gd, Sb, and Se elemental powders with a ratio of 1 : 1 : 1 in a vacuum-sealed evacuated quartz tube at 850 °C for 2 days. Then, the precursor was used as a source for CVT, which was performed with a temperature gradient from 1075 and 975 °C for two weeks. Millimeter-size single crystals with metal luster can be obtained, as shown in the inset of Fig. 1(a). The composition and structure analyses by energy-dispersive x-ray spectroscopy (EDS) and x-ray diffraction (XRD), respectively, have revealed an orthorhombic phase of Gd_2Se_3. The addition of Sb in the precursor is necessary to produce the desired sesqui-chalcogenides phase; otherwise, dichalcogenide $GdSe_2$ is produced. Nevertheless, the crystals obtained were found to be in a pure phase with no trace of Sb, according to EDS or XRD. Temperature-dependent magnetization was measured using a 7 T Magnetic Property Measurement System (MPMS3, Quantum Design). Field-dependent magnetization up to 9 T, electronic transport using a four-probe contact configuration, and heat capacity were measured using a Physical Property Measurement System (PPMS DynaCool, Quantum Design). The high-field magnetoresistance measurements up to 31 T were performed at the National High Magnetic Field Laboratory (NHMFL).

III. RESULTS AND DISCUSSION

Rietveld refinement of the XRD pattern for Gd_2Se_3 [Fig. 1(a)] resolves an orthorhombic lattice structure with a space group *Pnma* (i.e., α phase), as shown in Fig. 1(b). The extracted structural parameters are presented in Table I. To uncover the magnetic properties of α-Gd_2Se_3, we performed the temperature-dependent [$\chi(T)$] and field-dependent [$M(H)$] magnetization measurements. According to single crystal XRD, the natural cleavage plane of the single crystal is (201); therefore, the magnetic field was applied perpendicular [$H\perp(201)$] and parallel [$H//(201)$] to the (201) plane for magnetization measurements. The temperature dependence of susceptibility χ measured with 0.1 T magnetized field applied perpendicular [$H\perp(201)$] and parallel [$H//(201)$] to the (201) plane reveals clear magnetic transitions at 11 K, as shown in Figs. 2(a) and 2(b). Here, we denote susceptibility measured under $H\perp(201)$ and $H//(201)$ as $\chi_\perp$ and $\chi_{//}$, respectively. The very weak irreversibility between zero-field-cooling (ZFC) and field-cooling (FC) measurements at very low temperatures ($T < 4$ K) in both $\chi_\perp$ and $\chi_{//}$ [Fig. 2(b), inset] suggests an AFM ground state, which is further supported by the field dependence of magnetization, as will be shown later. The weak irreversibility might be attributed to weak ferromagnetism arising from magnetic fluctuations due

TABLE I. Structural parameters of Gd_2Se_3 at $T = 300$ K. Space group: *Pnma*; $a = 11.177(1)$ Å, $b = 4.049(4)$ Å, $c = 10.966(4)$ Å; $\alpha = \beta = \gamma = 90°$, $R_p = 4.87$, $R_{wp} = 4.64$.

Atoms	Wycoff	x	y	z
Gd1	4c	0.9901(3)	1/4	0.3117(5)
Gd2	4c	0.3046(4)	1/4	0.5042(1)
Se1	4c	0.0453(4)	1/4	0.8753(3)
Se2	4c	0.8763(8)	1/4	0.5585(9)
Se3	4c	0.2259(9)	1/4	0.1956(6)

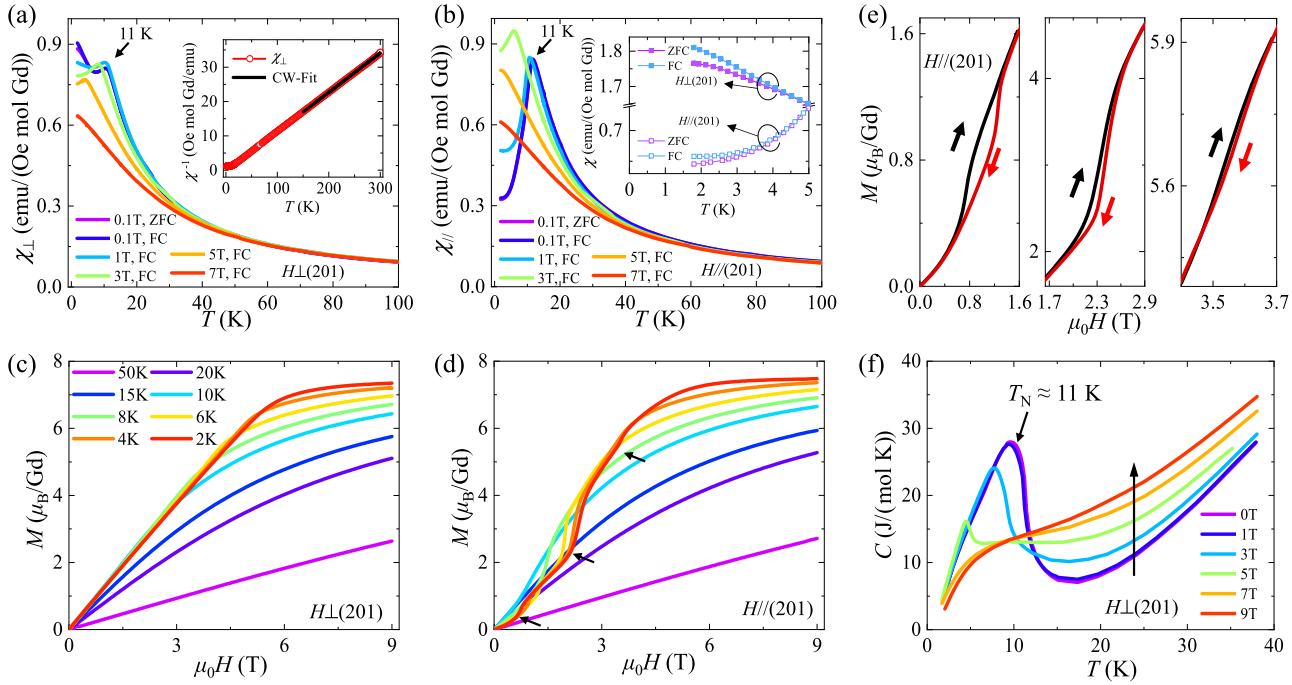

FIG. 2. Magnetic properties of α-Gd_2Se_3. (a) Temperature dependence of molar susceptibility of α-Gd_2Se_3 measured under $H\perp(201)$ magnetic fields from 0.1 to 7 T. Inset shows CW fit for the inverse susceptibility measured at 0.1 T. (b) Temperature dependence of molar susceptibility measured under various $H//(201)$ magnetic fields from 0.1 to 7 T. Inset shows enlarged view of ZFC and FC susceptibility below 5 K measured with 0.1 T field. Field dependence of magnetization with (c) out-of-plane $H\perp(201)$ and (d) in-plane $H//(201)$ magnetic fields at different temperatures. The same color code is used for panels (c) and (d) to distinguish each temperature. Arrows in panel (d) indicate metamagnetic transitions. Magnetic hysteresis of these metamagnetic transitions at 2 K are shown in panel (e). (f) Temperature dependence of heat capacity of α-Gd_2Se_3 measured under various magnetic fields applied along the out-of-plane [$H \perp (201)$ plane] direction from 0 to 9 T.

to the strong competition between AFM and ferromagnetic (FM) interactions, which has been theoretically revealed for the case of α-Gd_2Te_3 [58]. Such low-temperature magnetic fluctuation can be important in electronic transport because it can act as a source for charge carrier scattering and affect transport significantly. The Néel temperature T_N of the AFM transition shifts to a lower temperature upon increasing the magnetic field. Eventually, T_N becomes unobservable down to $T = 2$ K above 5 and 3 T fields for perpendicular, i.e., $H\perp(201)$ [Fig. 2(a)], and parallel, i.e., $H//(201)$ [Fig. 2(b)] directions, respectively. Such field suppression of T_N is also observed in the sulfide and telluride sibling compounds α-Gd_2S_3 [62] and α-Gd_2Te_3 [58] as well as other rare-earth materials [63,64]. The low field (0.1 T) $\chi_{//}$ exhibits a much sharper drop below T_N as compared with $\chi_\perp$ [Figs. 2(a) and 2(b)], suggesting that the magnetic easy axis may be within or almost within the (201) plane.

In the paramagnetic (PM) state, the inverse of susceptibility $1/\chi(T)$ displays a linear temperature dependence well above T_N ($T > 150$ K) [Fig. 2(a), inset], which can be described by the modified Curie-Weiss (CW) model $\chi = \chi_0 + C/(T - \theta_{cw})$, where χ_0, C, and θ_{cw} represent the temperature-independent susceptibility, Curie constant, and Weiss temperature, respectively. The CW fitting yielded an effective moment $\mu_{eff} = \sqrt{3k_BC/N_A}$ of 8.34μ_B, where N_A is Avogadro's number and k_B is the Boltzmann constant. Such a value is very close to the theoretical moment of 7.93μ_B for Gd^{3+} ions with a $4f^7$ configuration and consistent with other reported compounds containing Gd^{3+}, such as the sibling compound α-Gd_2Te_3 [58] and other Gd-based compounds such as GdPS [59]. Furthermore, the fitting yields a positive $\theta_{cw} \approx 1.168$ K, which appears to be inconsistent with the AFM ground state of α-Gd_2Se_3 but might be explained by the weak ferromagnetic fluctuation due to competing AFM and FM interactions [65,66], as mentioned above. Further experimental and theoretical efforts are needed to determine the magnetic structure and clarify the enhanced μ_{eff} and positive θ_{cw} in α-Gd_2Se_3.

The AFM ground state is further supported by the isothermal magnetization measurements, which display a linear field dependence near zero fields at temperatures below $T_N \approx 11$ K, as shown in Figs. 2(c) and 2(d). Additional features can be observed at high fields. For $H\perp(201)$, the magnetization tends to saturate above 5 T at $T = 2$ K [Fig. 2(c)]. A similar tendency is also seen when $H//(201)$ [Fig. 2(d)]. As will be shown later, our high-field magnetotransport reveals a complete saturation under $H\perp(201)$ around 16 T near 2 K. Though perfect moment saturation may not be achieved in magnetization measurements up to 9 T, the moment reaches 7.48μ_B and 7.36μ_B per Gd for $H//(201)$ and $H\perp(201)$ respectively, indicating strong polarization of the Gd moments. In addition to moment polarization under high field, one striking feature in magnetization is the three metamagnetic transitions at lower fields, which are present for $H//(201)$ but absent for $H\perp(201)$, as indicated by black arrows in Fig. 2(d). Interestingly, magnetic hysteresis is observed for these metamagnetic transitions around 0.85, 2.35, and 3.55 T at $T = 2$ K, as shown in Fig. 2(e). This implies the development of magnetic domains that might be associated with FM correlations from the canted

moment, which is likely caused by the competition between AFM and FM interactions, as stated above. These transitions resemble spin-flop (SF) transitions in AFM material such as $MnPS_3$ and $NiPS_3$ [67,68], which has also been observed in α-Gd_2Te_3 [58]. Because SF transitions in AFM materials are caused by the moments rotation, which is driven by the magnetic field parallel to the magnetic easy axis, our observations indicate that the magnetic easy axis for α-Gd_2Se_3 is within or close to the (201) plane, which is consistent with that observed from temperature-dependent susceptibility measurements, as discussed above. A similar scenario has also been observed in α-Gd_2S_3 [62] and α-Gd_2Te_3 [58]. It is not clear how multiple SF transitions can occur in one material. Possible mechanisms include the presence of multiple magnetic lattices or complicated magnetic structures with noncollinear moments. More direct experimental probes, such as neutron scattering, are needed to clarify the nature of these metamagnetic transitions.

The comparison of various α-$Gd_2(S, Se, Te)_3$ sesquichalcogenides provides some insight into the nature of magnetism in those materials. In addition to α-Gd_2Se_3, α-Gd_2S_3 also displays multiple metamagnetic transitions at lower fields and spin polarization around 11 to 12 T [62], while α-Gd_2Te_3 exhibits only one spin flop transition without moment polarization up to a 9 T field [58]. Such differences might be attributed to the nature of the AFM ground states in this family of materials. Antiferromagnetism in α-Gd_2Te_3 has been predicted to be stabilized mainly by the $4f$ $Gd^{3+} - 5p$ $Te^{2-} - 4f$ Gd^{3+} superexchange interactions [58]. A similar scenario can be expected in α-Gd_2S_3 and α-Gd_2Se_3, where magnetism could be governed by the $4f$ $Gd^{3+} - 5p$ $(S \text{ or } Se)^{2-} - 4f$ Gd^{3+} superexchange interactions. The dominant role of $Gd^{3+} - X^{2-} - Gd^{3+}$ (X = S, Se, or Te) superexchange interaction is supported by the variation of T_N magnitude, which systematically increases from $T_N \approx 10$ K in α-Gd_2S_3 [54,62] to $T_N \approx 11$ K in α-Gd_2Se_3 (this work) and to $T_N \approx 15$ K in α-Gd_2Te_3 [58], which can be explained by the enhanced superexchange interaction due to stronger orbital overlap with expanded p-orbitals from S to Se and to Te. Therefore, with enhanced superexchange, α-Gd_2Te_3 possesses a more robust AFM ground state and thus needs a higher field to induce moment reorientation and FM polarization.

Heat capacity measurements also provide useful information about magnetism. As shown in Fig. 2(f), a broad heat capacity peak centered at 11 K is consistent with the AFM transition temperature in the susceptibility measurements. With the application of the magnetic field, the heat capacity peak is suppressed to lower temperatures, which agrees well with the field suppression for AFM transition seen in susceptibility measurements [Figs. 2(a) and 2(b)]. Interestingly, heat capacity in the PM state is enhanced strongly by the magnetic field, as indicated by the arrow in Fig. 2(f). Such enhancement is distinct from some other rare-earth-based AFM materials such as LnSnGe (Ln = Gd, Tb, and Er) [69] and SmSbTe [70], indicating very strong magnetic correlations in the PM state, which is also supported by the observation of spin polarization above T_N [Figs. 2(c) and 2(d)]. Such strong magnetic correlations above T_N are also probed in transport measurements, as will be discussed below.

With the characterization of magnetism, the interplay of magnetism and transport can be revealed by magnetotransport measurements. As shown in Fig. 3(a), the temperature dependence of resistivity displays overall metallic behavior, which shows decreased resistivity upon cooling. Over the entire temperature range (2–300 K), the resistivity is in the order of 1 mΩ cm, implying that α-Gd_2Se_3 might not be a good metal. Such a resistivity value is comparable to α-Gd_2Te_3, which has been proposed to be a semimetal [58], whereas the sulfide compound α-Gd_2S_3 is a semiconductor [54]. In addition to the orthorhombic α phase studied in this work, the cubic phase has been more extensively investigated, which can display both metallic and nonmetallic transport behavior depending on the Gd vacancies [9,60,71]. For our α-Gd_2Se_3, at zero field, a sharp resistivity peak at $T_N \approx 11$ K can be observed. The resistivity peak is suppressed with the application of a perpendicular magnetic field [$H \perp (201)$] and vanishes when $\mu_0 H \geqslant 7$ T, consistent with the suppression of T_N seen in magnetic susceptibility and heat capacity measurements mentioned above. Furthermore, above 130 K, resistivity displays a linear temperature dependence that is not affected by the magnetic field, as shown in the inset of Fig. 3(a).

The suppression of the resistivity peak by the magnetic field leads to remarkable negative magnetoresistance (MR), which can be better visualized in the field dependence for resistivity, as shown in Fig. 3(b). Here, the MR is normalized to the zero-field resistivity value, i.e., $\text{MR} = \frac{\rho(H) - \rho(0)}{\rho(0)}$. With this definition, large MR $\approx 65\%$ can be observed at 10 K and 9 T. At $T = 2$ K, MR is reduced to 54%, with a tendency toward saturation approaching 9 T. Upon extending the magnetic field to 31 T at the NHMFL, complete MR saturation reaching 57% was achieved around 16.7 T at 2.2 K. Lower temperature to 1.5 K, the saturation MR is reduced to 49% around 12.5 T, as shown in the inset of Fig. 3(b). The temperature dependence of MR magnitude at 9 T field (MR_{9T}) is summarized in Fig. 3(c), from which the maximum MR near T_N (= 11 K) is clearly seen. Above T_N, MR gradually reduces with rising temperature, reaching $\approx$12% at 50 K and becoming hardly observable above 200 K. Those observations are reproducible in multiple samples, as evinced by the consistent results obtained from the two different samples for the low-field [Fig. 3(b), main panel] and high-field [Fig. 3(b), inset] measurements.

The substantial negative MR in α-Gd_2Se_3 near T_N has also been observed in other AFM materials, such as $CeAgAs_2$ [72], $EuIn_2As_2$ [73], $Eu_{14}MnBi_{11}$ [74], and $Eu_3Ni_4Ga_4$ [75]. Generally, the negative MR can arise from various mechanisms, such as magnetic-field-induced modification of electronic band structures [76–78], the Kondo effect [79], weak localization [80,81], and chiral anomaly [82–85]. The change in electronic structure should lead to strong modifications to the carrier density, which can be probed by the Hall effect [76,86]. In α-Gd_2Se_3, however, as shown in the inset of Fig. 3(c), the Hall resistivity $\rho_{yx}(H)$ does not exhibit a strong deviation from a linear field, implying an almost unchanged electronic structure under a magnetic field. Furthermore, the carrier density extracted from the slope of $\rho_{yx}(H)$ displays rather weak temperature dependence from 2 to 300 K [Fig. 3(c)], suggesting that the AFM transition may not notably change the band structure. Near zero field, $\rho_{yx}(H)$ displays a very weak

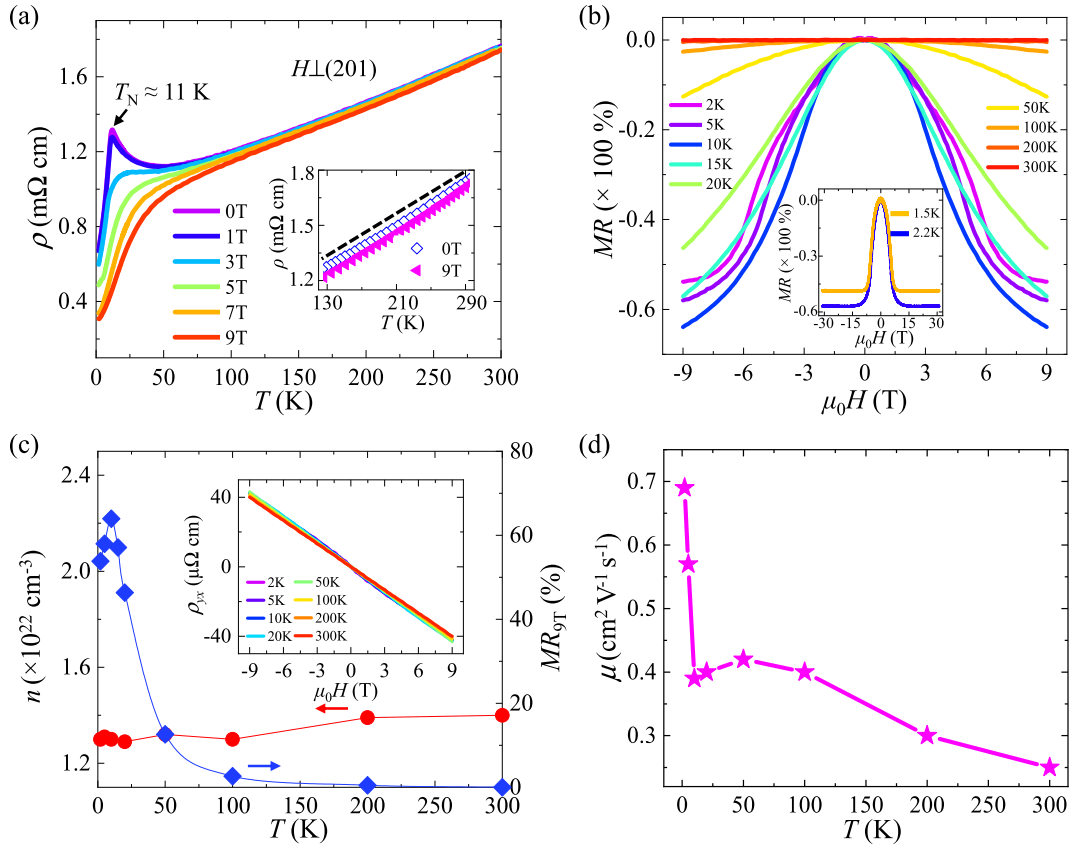

FIG. 3. Magnetotransport properties of Gd_2Se_3. (a) Temperature dependence of resistivity of Gd_2Se_3 under various magnetic fields applied perpendicularly [$H\perp(201)$]. Inset shows linear temperature dependence for resistivity at high temperatures under 0 and 9 T fields. The black dashed lines are guides for the eyes. (b) Normalized MR at different temperatures. Inset shows high-field MR measured up to 31 T at 1.5 and 2.2 K. (c) Temperature dependence of carrier concentration extracted from Hall effect (n, left vertical axis) and magnitude of MR at 9 T field (MR_{9T}, right vertical axis). Inset shows field dependence of Hall resistivity at different temperatures. (d) Temperature dependence of carrier mobility μ extracted using the single-band model.

nonlinearity below 20 K. Since magnetization and ρ_{yx} under $H\perp(201)$ do not evolve coincidently with the magnetic field, such nonlinearity is less likely to originate from the anomalous Hall effect. Hence, it is better attributed to a multiband effect. In general, the multiband effect is manifested in both longitudinal ρ_{xx} and transverse (ρ_{yx}) resistivity, producing a nearly H^2-like field dependence for $\rho_{xx}(H)$ and nonlinearity in $\rho_{yx}(H)$. Providing the existence of multiple correlated fitting parameters, the carrier density and mobility for each band should be obtained via simultaneous fitting of both $\rho_{xx}(H)$ and $\rho_{yx}(H)$ to the multiband model. However, given longitudinal resistivity $\rho_{xx}(H)$ for α-Gd_2Se_3 exhibits a negative MR that is not described by the multiband model, it is thus not possible to obtain reliable carrier densities and mobilities. Nevertheless, providing that the nonlinearity in $\rho_{yx}(H)$ is rather weak, electronic transport in α-Gd_2Se_3 is dominated by one band. Therefore, the carrier density n can be estimated from the single-band model, as shown in Fig. 3(c), from which the carrier mobility can be calculated via $\mu = 1/(ne\rho_{xx})$, as presented in Fig. 3(d).

Similarly, the Kondo effect due to the screening of dilute magnetic moments by carriers can also be ruled out because it should lead to low-temperature resistivity upturn with a logarithmic temperature dependence [79,87–89], which is not observed in α-Gd_2Se_3. In addition, the observed large negative MR is much higher than those observed for the Kondo system [89–91]. The weak localization can be excluded as well. This effect is caused by the enhanced backscattering rate due to the constructive interference of the time-reversal backscattering carrier paths. Applying a magnetic field suppresses the quantum interference and lowers the backscattering rate, leading to negative MR [80,81]. However, MR is expected to saturate quickly with the magnetic field at low temperatures owing to the efficient suppression of quantum interference, which is not observed in α-Gd_2Se_3. The negative MR in α-Gd_2Se_3 should not be ascribed to chiral anomaly either. This phenomenon, i.e., imbalance of chiral fermions, arises from the charge pumping between a pair of Weyl cones under parallel electrical and magnetic fields [82,83], and hence it is sensitive to the directions of the magnetic field. Figure 4(a) shows the MR at 2 K measured at various field orientations. Strong MR ≈54% at 9 T can be observed for all field orientations from H // I ($\theta = 90°$) and $H \perp I$ ($\theta = 0°$), indicating that the chiral anomaly is not applicable.

With ruling out the other mechanisms, the most likely origin for the strong negative MR in α-Gd_2Se_3 is the suppression of magnetic scattering by the field. Our transport

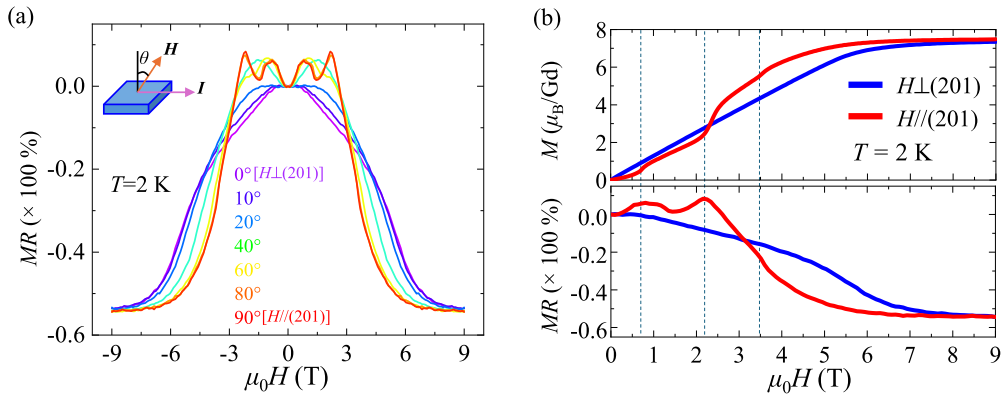

FIG. 4. (a) MR of Gd_2Se_3 at $T = 2$ K under different magnetic-field orientations. The measurement setup is shown in the inset. (b) Comparison of the field-driven transitions between magnetization (upper panel) and MR (lower panel) under $H\perp(201)$ and $H//(201)$ fields at $T = 2$ K, which are reproduced from Figs. 2(c), 2(d), and 4(a). The vertical dashed lines denote the metamagnetic transition fields.

measurements reveal a very strong interplay between magnetism and electronic transport. As stated above, the temperature dependence for resistivity at zero magnetic field displays a sharp peak at $T_N \approx 11$ K [Fig. 3(a)]. This can be understood in terms of the enhanced magnetic scattering near the magnetic ordering temperature where the spin fluctuations are the strongest. In fact, the temperature-dependent resistivity at zero magnetic field starts to develop an upturn at 55 K, which is much higher than T_N and implies sizeable magnetic scattering above T_N. Such a scenario is also consistent with the strong field-induced heat capacity enhancement above T_N mentioned above [Fig. 2(f)]. Therefore, resistivity reduction due to the suppression of magnetic fluctuations by the magnetic field is expected. Such suppression should be the most significant at T_N and consequently leads to the strongest negative MR near T_N, as observed in our magnetotransport measurements [Figs. 3(b) and 3(c)]. Above T_N, MR is also reduced upon heating because the thermal energy randomizes magnetic-moment orientations, and it becomes more difficult to polarize these moments by the magnetic field. However, providing strong magnetic correlations up to 55 K, as discussed above, MR retains a remarkable value of 46% at 20 K and remains 12% at 50 K. The persistence of substantial magnetic correlations well above the magnetic transition temperature in Gd_2Se_3 appears to be consistent with other magnetic compounds containing Gd, such as GdPS [59]. Additionally, temperature-dependent mobility also supports the scenario of magnetic scattering. As shown in Fig. 3(d), at low temperatures, mobility μ increases because of suppressing magnetic fluctuations. μ reaches a local minimum around T_N due to the strong spin scattering with the presence of intense magnetic fluctuations. Upon increasing the temperature, the spin scattering is suppressed, but the electron-phonon interaction becomes strengthened. The competition of the two mechanisms leads to nonmonotonic temperature dependence for mobility for $T > T_N$. Mobility slightly enhances up to $\approx$50 K where spin fluctuations start to develop, while it drops at higher temperatures when electron-phonon interactions dominate.

In addition to the temperature dependence, the field dependence of resistivity provides additional support. As shown in Fig. 3(b), for $H\perp(201)$, though MR at 2 K is lower than that at T_N, its saturation behavior resembles that of the magnetization saturation [Fig. 2(c)]. This should be attributed to the nearly complete suppression of spin fluctuations when magnetic moments are fully polarized. Similar low-temperature saturation behavior in MR [Fig. 4(a)] and magnetization [Fig. 2(d)] is also observed under the in-plane $H//(201)$ field. The multiple peak-like features in MR for $H//(201)$ in Fig. 4(a) should be ascribed to metamagnetic SF transitions. Fig. 4(b) presents the field dependence for magnetization and MR under $H\perp(201)$ and $H//(201)$ at 2 K. The metamagnetic transitions at 0.85 and 2.35 T for $H//(201)$ are accompanied by positive MR, whereas the metamagnetic transition at 3.55 T is too weak to develop a clear positive MR but rather exhibits a weak slope change in MR. On the other hand, for $H\perp(201)$, where the metamagnetic transition is not present, MR lacks any other feature exhibiting high field saturation. These observations can be understood in terms of the spin scattering. Upon applying a magnetic field near an SF field, the spin scattering is strong due to strong spin fluctuations in the vicinity of the SF transition. Furthermore, increasing the field suppresses spin fluctuations and reduces scattering. Thus, a peak-like feature and positive MR is observed near SF transition fields.

The angular MR (AMR) is also consistent with the scenario of spin scattering. Figs. 5(a) and 5(b) show the angular dependence for resistivity measured at fixed magnetic fields from 1 to 9 T at $T = 2$ K (AFM state) and 15 K (PM state), respectively. At 2 K, the low field (1 and 2 T) AMR displays relatively complicated angular dependence with multiple peaks, with an overall two-fold anisotropy with the maxima and minima at $H//(201)$ and $H\perp(201)$, respectively. Such complicated MR anisotropy should be caused by the multiple metamagnetic transitions that are sensitive to magnetic field orientation, as seen in the field-dependent MR in Fig. 4(a). The low-field MR reaches a maximum when the field is applied along the magnetic easy axis [i.e., $H//(201)$], which can be understood in terms of enhanced spin scattering at an SF transition, as discussed above. With an increasing magnetic field, an AMR dip at $H//(201)$ starts to develop, causing a four-fold-like AMR anisotropy at 3 T. Such an AMR dip becomes more significant upon further increasing the magnetic field, leading to AMR minima at $H//(201)$ above 5 T, as shown in Fig. 5(a). This can be attributed to the strong

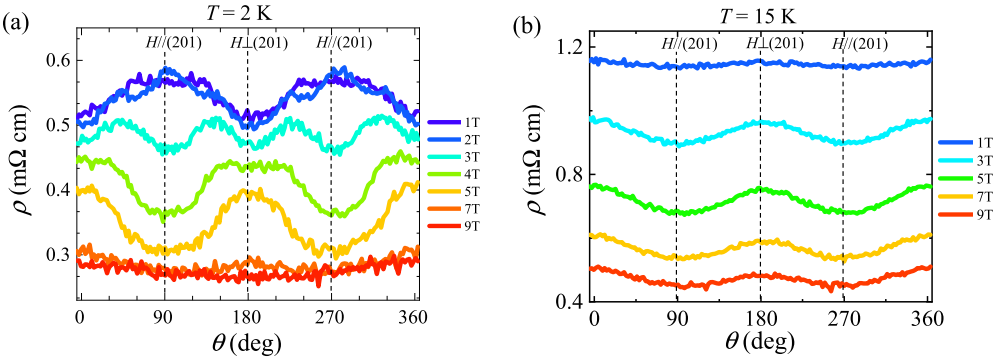

FIG. 5. Angular dependence of resistivity of α-Gd_2Se_3 single crystal below [2 K, panel (a)] and above [15 K, panel (b)] T_N measured under different magnetic fields. The dashed lines denote $H//(201)$ and $H\perp(201)$ field orientations.

suppression of spin scattering when $H//(201)$. Unlike the perpendicular field $H\perp(201)$, the in-plane field $H//(201)$ induces SF transitions with which the FM component develops more rapidly, leading to a strong increase and quick saturation of magnetization at higher fields. Therefore, the spin scattering is more suppressed for $H//(201)$ at higher fields, causing the AMR to change anisotropy with the field. At temperatures above T_N, a similar two-fold AMR anisotropy with minima at $H//(201)$ remains observable at 15 K for various applied magnetic fields (Fig. 5b), which agrees with the presence of strong magnetic correlations above T_N mentioned above and further supports the scenario of negative MR due to spin scattering.

IV. CONCLUSION

In conclusion, we have successfully synthesized the single crystal of the orthorhombic phase of Gd_2Se_3 by chemical vapor transport and studied its transport, magnetic, and calorimetric properties. We found that α-Gd_2Se_3 possesses an AFM order below $T_N \approx 11$ K, which can be driven into a polarized FM state at higher fields. In the PM state, magnetic fluctuations remain strong. The transport measurements reveal metallic-like behavior and large negative MR near T_N, which should be attributed to the suppression of spin scatterings. Overall, α-Gd_2Se_3 behaves as an intermediate material between nonmetallic α-Gd_2S_3 and metallic α-Gd_2Te_3 in terms of magnetic properties, displaying strong modification of electron transport by magnetism. Therefore, magnetism and transport are expected to be highly tunable by various approaches, such as chemical substitution, pressure, and strain, which might provide a versatile platform for spintronics applications.

ACKNOWLEDGMENTS

This work was primarily (synthesis, heat capacity, magnetization up to 9 T, and transport) supported by the U.S. Department of Energy, Office of Science, Basic Energy Sciences program under Grant No. DE-SC0022006. M.M. and R.B. acknowledge μ-ATOMS, an Energy Frontier Research Center funded by DOE, Office of Science, Basic Energy Sciences, under Award DE-SC0023412 for part of magnetism and structural analyses. J.S. acknowledges support from NIH under Award P20GM103429 for XRD. J.H. acknowledges the MonArk NSF Quantum Foundry supported by the National Science Foundation Q-AMASE-i program under NSF Award No. DMR-1906383 for 7T magnetization study using MPMS3 SQUID. High-field magnetotransport was performed at the National High Magnetic Field Laboratory, which is supported by National Science Foundation Cooperative Agreement No. DMR-2128556 and the State of Florida.

[1] K. A. Gschneidner Jr, Preparation and processing of rare earth chalcogenides, J. Mater. Eng. Perform. **7**, 656 (1998).

[2] C. Witz, D. Huguenin, J. Lafait, S. Dupont, and M. L. Theye, Comparative optical studies of Ce_2S_3 and Gd_2S_3 compounds, J. Appl. Phys. **79**, 2038 (1996).

[3] F. Qin, S. A. Nikolaev, A. S., M. Wood, Y. Zhu, X. Tan, U. Aydemir, Y. Ren, Q. Yan, L. Hu, and G. J. Snyder, Crystal structure and atomic vacancy optimized thermoelectric properties in gadolinium selenides, Chem. Mater. **32**, 10130 (2020).

[4] Y. Iyeiri, T. Okumura, C. Michioka, and K. Suzuki, Magnetic properties of rare-earth metal tritellurides RTe_3(R = Ce, Pr, Nd, Gd, Dy), Phys. Rev. B **67**, 144417 (2003).

[5] C. Michioka, K. Fukushima, K. Suzuki, and K. Yoshimura, Physical Properties of RSe_{2-x}(R = Ce, Nd, Sm and Gd) and Rb_xGdSe_{3-y}, J. Phys. Chem. Solids **66**, 1579 (2005).

[6] H. Poddig, T. Donath, P. Gebauer, K. Finzel, M. Kohout, Y. Wu, P. Schmidt, and T. Doert, Rare earth metal polytellurides $RETe_{1.8}$(RE = Gd, Tb, Dy)–directed synthesis, crystal and electronic structures, and bonding features: Rare earth metal polytellurides $RETe_{1.8}$ (RE = Gd, Tb, Dy) – directed synthesis, crystal and electronic structures, and bonding features, Z. Für Anorg. Allg. Chem. **644**, 1886 (2018).

[7] P. N. Kumta and S. H. Risbud, Rare-earth chalcogenides: An emerging class of optical materials, J. Mater. Sci. **29**, 1135 (1994).

[8] Z. Charifi, H. Baaziz, Y. Saeed, A. H. Reshak, and F. Soltani, The effect of chalcogen atom on the structural, elastic, and high-pressure properties of XY compounds (X = La, Ce, Eu, and Y = S, Se, and Te): An *ab initio* study: Effect of chalcogen

atom on structural, elastic, and high-pressure properties, Phys. Status Solidi B **249**, 18 (2012).
[9] R. C. Vickery and H. M. Muir, Thermoelectric properties of rare earth chalcogenides, Adv. Energy Convers. **1**, 179 (1961).
[10] J. Flahaut, Chapter 31 Sulfides, selenides and tellurides, in *Handbook on the Physics and Chemistry of Rare Earths*, edited by K. A. J. Gschneider and L. Eyring (North-Holland Publishing Company, Amsterdam, 1979), Vol. 4, pp. 1–88.
[11] S. Cotton, *Lanthanide and Actinide Chemistry* (Wiley, Rutland, UK, 2006).
[12] J. M. Honig, On the band structure of rare earth chalcogenides and pnictides, J. Solid State Chem. **1**, 19 (1969).
[13] Z. Zhang, H. Zhao, C. Zhang, F. Luo, and Y. Du, Rare-earth-incorporated low-dimensional chalcogenides: Dry-method syntheses and applications, InfoMat **2**, 466 (2020).
[14] M. Zeer, D. Go, P. Schmitz, T. G. Saunderson, H. Wang, J. Ghabboun, S. Blügel, W. Wulfhekel, and Y. Mokrousov, Promoting p-based Hall effects by $p-d-f$ hybridization in Gd-based dichalcogenides, Phys. Rev. Res. **6**, 013095 (2024).
[15] F. J. Reid, L. K. Matson, J. F. Miller, and R. C. Himes, Electrical conduction in rare-earth monoselenides and monotellurides and their alloys, J. Phys. Chem. Solids **25**, 969 (1964).
[16] R. Didchenko and F. P. Gortsema, Some electric and magnetic properties of rare earth monosulfides and nitrides, J. Phys. Chem. Solids **24**, 863 (1963).
[17] A. Chatterjee, A. K. Singh, and A. Jayaraman, Pressure-induced electronic collapse and structural changes in rare-earth monochalcogenides, Phys. Rev. B **6**, 2285 (1972).
[18] C. J. M. Rooymans, High pressure phase transition of europium telluride, Solid State Commun. **3**, 421 (1965).
[19] V. Srivastava, A. K. Bandyopadhyay, P. K. Jha, and S. P. Sanyal, High pressure phase transition and elastic properties of cerium chalcogenides and pnictides, J. Phys. Chem. Solids **64**, 907 (2003).
[20] V. Srivastava, S. Bhajanker, and S. P. Sanyal, High pressure effect on structural and mechanical properties of some LnO (Ln = Sm, Eu, Yb) compounds, Phys. B Condens. Matter **406**, 2158 (2011).
[21] S. Singh, R. Singh, and A. Gour, Phase transition in CeSe, EuSe and LaSe under high pressure, Open Phys. **5**, 576 (2007).
[22] N. I. Atallah, M. El-Kemary, F. Pascale, and K. E. El-Kelany, Extraordinary piezoelectric effect induced in two-dimensional rare earth monochalcogenides via reducing system dimensionality, J. Materiomics **9**, 72 (2023).
[23] H. Guo, J. Zhao, C. Chen, S. Li, W. Jiang, X. Tian, and S. A. Yang, Nonsymmorphic nodal-line metals in the two-dimensional rare earth monochalcogenides MX (M = Sc, Y: X = S, Se, Te), J. Mater. Sci. **55**, 14883 (2020).
[24] N. V. Podberezskaya, S. A. Magarill, N. V. Pervukhina, I. G. Vasilieva, and S. V. Borisov, Crystal-chemical aspects of the structural similarity of rare earth polychalcogenides $LnX_{2-x}(x = 0-0.25)$, J. Struct. Chem. **37**, 963 (1996).
[25] J. Gjerde and R. A. Jishi, Hyperbolic behavior and antiferromagnetic order in rare-earth tellurides, Cryst. **12**, 1839 (2022).
[26] T. Doert and C. J. Müller, Binary polysulfides and polyselenides of trivalent rare-earth metals, in *Reference Module in Chemistry, Molecular Sciences and Chemical Engineering* (Elsevier, 2016), p. B9780124095472115525.
[27] K. Yumigeta, Y. Attarde, J. Kopaczek, M. Y. Sayyad, Y. Shen, M. Blei, S. T. Rajaei Moosavy, Y. Qin, R. Sailus, and S. Tongay, The phononic and charge density wave behavior of entire rare-earth tritelluride series with chemical pressure and temperature, APL Mater. **10**, 111112 (2022).
[28] Y. S. Shin, C. W. Han, B. H. Min, H. J. Lee, C. H. Choi, Y. S. Kim, D. L. Kim, and Y. S. Kwon, Anisotropic magnetization in RTe_2 (R: Ce, Pr, Gd and Sm), Phys. B Condens. Matter **291**, 225 (2000).
[29] J. Yin, C. Wu, L. Li, J. Yu, H. Sun, B. Shen, B. A. Frandsen, D.-X. Yao, and M. Wang, Large negative magnetoresistance in the antiferromagnetic rare-earth dichalcogenide $EuTe_2$, Phys. Rev. Mater. **4**, 013405 (2020).
[30] E. DiMasi, B. Foran, M. C. Aronson, and S. Lee, Stability of charge-density waves under continuous variation of band filling in $LaTe_{2-x}Sb_x(0 \leqslant x \leqslant 1)$, Phys. Rev. B **54**, 13587 (1996).
[31] E. Lee, D. H. Kim, J. D. Denlinger, J. Kim, K. Kim, B. I. Min, B. H. Min, Y. S. Kwon, and J.-S. Kang, Angle-resolved and resonant photoemission spectroscopy study of the Fermi surface reconstruction in the charge density wave systems $CeTe_2$ and $PrTe_2$, Phys. Rev. B **91**, 125137 (2015).
[32] X. Cai, Z. Xu, R. An, J. Wu, S.-H. Ji, N. Li, and X. Chen, Charge density waves in $GdTe_2$ thin films, J. Phys. Chem. C **127**, 10730 (2023).
[33] P. Walmsley, S. Aeschlimann, J. A. W. Straquadine, P. Giraldo-Gallo, S. C. Riggs, M. K. Chan, R. D. McDonald, and I. R. Fisher, Magnetic breakdown and charge density wave formation: A quantum oscillation study of the rare-earth tritellurides, Phys. Rev. B **102**, 045150 (2020).
[34] K. Yumigeta, Y. Qin, H. Li, M. Blei, Y. Attarde, C. Kopas, and S. Tongay, Advances in rare-earth tritelluride quantum materials: Structure, properties, and synthesis, Adv. Sci. **8**, 2004762 (2021).
[35] P. T. Yang, Z. Y. Liu, K. Y. Chen, X. L. Liu, X. Zhang, Z. H. Yu, H. Zhang, J. P. Sun, Y. Uwatoko, X. L. Dong, K. Jiang, J. P. Hu, Y. F. Guo, B. S. Wang, and J.-G. Cheng, Pressured-induced superconducting phase with large upper critical field and concomitant enhancement of antiferromagnetic transition in $EuTe_2$, Nat. Commun. **13**, 2975 (2022).
[36] D. A. Zocco, J. J. Hamlin, K. Grube, J.-H. Chu, H.-H. Kuo, I. R. Fisher, and M. B. Maple, Pressure dependence of the charge-density-wave and superconducting states in $GdTe_3$, $TbTe_3$, and $DyTe_3$, Phys. Rev. B **91**, 205114 (2015).
[37] J. J. Hamlin, D. A. Zocco, T. A. Sayles, M. B. Maple, J.-H. Chu, and I. R. Fisher, Pressure-induced superconducting phase in the charge-density-wave compound terbium tritelluride, Phys. Rev. Lett. **102**, 177002 (2009).
[38] J. B. He, P. P. Wang, H. X. Yang, Y. J. Long, L. X. Zhao, C. Ma, M. Yang, D. M. Wang, X. C. Shangguan, M. Q. Xue, P. Zhang, Z. A. Ren, J. Q. Li, W. M. Liu, and G. F. Chen, Superconductivity in Pd-intercalated charge-density-wave rare earth poly-tellurides $RETe_n$, Supercond. Sci. Technol. **29**, 065018 2016.
[39] J. A. W. Straquadine, F. Weber, S. Rosenkranz, A. H. Said, and I. R. Fisher, Suppression of charge density wave order by disorder in Pd-intercalated $ErTe_3$, Phys. Rev. B **99**, 235138 (2019).
[40] W. H. Zachariasen, Crystal chemical studies of the $5f$-series of elements. VI. The Ce_2S_3-Ce_3S_4 type of structure, Acta Crystallogr. **2**, 57 (1949).
[41] C. M. Marin, L. Wang, J. R. Brewer, W.-N. Mei, and C. L. Cheung, Crystalline α-Sm_2S_3 nanowires: Structure and optical

properties of an unusual intrinsically degenerate semiconductor, J. Alloys Compd. **563**, 293 (2013).

[42] S. Roméro, A. Mosset, J.-C. Trombe, and P. Macaudière, Low-temperature process of the cubic lanthanide sesquisulfides:Remarkable stabilization of the γ-Ce_2S_3 phasei, J. Mater. Chem. **7**, 1541 (1997).

[43] C. T. Prewitt and A. W. Sleight, Structure of gadolinium sesquisulfide, Inorg. Chem. **7**, 1090 (1968).

[44] J. C. Trombe and M. Verelst, Stabilization of the γ-Ce_2S_3 phase, J. Alloys Compd. **323–324**, 66 (2001).

[45] M. Kanazawa, L. Li, T. Kuzuya, K. Takeda, S. Hirai, Y. Higo, T. Shinmei, T. Irifune, and C. Sekine, High-pressure and high-temperature synthesis of heavy lanthanide sesquisulfides Ln_2S_3(Ln = Yb and Lu), J. Alloys Compd. **736**, 314 (2018).

[46] T. Schleid and F. Lissner, A-Pr_2S_3, D-Ho_2S_3 and E-Yb_2S_3: Synthesis and single crystal structure investigations, Zeitschrift fr Naturforschung **51**, 733 (1996).

[47] D. Damien, A. Wojakowski, and W. Muller, α and β curium sesquisulfides, Inorg. Nucl. Chem. Lett. **12**, 533 (1976).

[48] A. Aruga, S. Tsujimi, and I. Nakai, Crystal structure of samarium sesquisulfide, α-Sm_2S_3, Anal. Sci. **12**, 151 (1996).

[49] J. Kończyk, P. Demchenko, O. Bodak, G. Demchenko, B. Marciniak, W. Prochwicz, L. Muratova Crystal structure of δ-Tm_2S_3, Chem. Met. Alloys **1**, 38 (2008).

[50] S. Ebisu, T. Nagata, K. Fuji, and Y. Shibayama, Magnetism in α-R_2S_3(R = Pr and Nd) single crystals, J. Phys. Conf. Ser. **568**, 042003 (2014).

[51] S. Ebisu, K. Koyama, T. Horikoshi, M. Kokita, and S. Nagata, Extremely broad hysteresis in the magnetization process of α-Dy_2S_3 single crystal induced by high field cooling, J. Phys. Conf. Ser. **400**, 032010 (2012).

[52] S. Ebisu, K. Koyama, H. Omote, and S. Nagata, High field magnetization processes in single crystals of α-Tb_2S_3 and α-Dy_2S_3, J. Phys. Conf. Ser. **150**, 042027 (2009).

[53] S. Ebisu, Y. Ushiki, and S. Takahashi, Specific-heat study on successive magnetic transitions in α-Dy_2S_3 single crystals under magnetic fields, J. Korean Phys. Soc. **63**, 571 (2013).

[54] S. Ebisu, Y. Iijima, T. Iwasa, and S. Nagata, Antiferromagnetic transition and electrical conductivity in α-Gd_2S_3, J. Phys. Chem. Solids **65**, 1113 (2004).

[55] S. Ebisu, H. Omote, and S. Nagata, Drastic change of the electrical resistivity related to the novel magnetic phase transition in α-Sm_2S_3, J. Phys. Conf. Ser. **200**, 092005 (2010).

[56] M. Folchnandt and T. Schleid, Single crystals of C-La_2Se_3, C-Pr_2Se_3, and C-Gd_2Se_3 with cation-deficient Th_3P_4-type structure, Z. Für Anorg. Allg. Chem. **627**, 1411 (2001).

[57] A. R. Kopan' and N. P. Gorbachuk, The thermal capacity and enthalpy of gadolinium sesquiselenide over a wide temperature range, Powder Metall. Met. Ceram. **45**, 153 (2006).

[58] I. P. Muthuselvam, R. Nehru, K. R. Babu, K Saranya, S. N. Kaul, S.-M. Chen, W.-T. Chen, Y. Liu, G.-Y. Guo, F. Xiu, and R. Sankar, Gd_2Te_3: An antiferromagnetic semimetal, J. Phys. Condens. Matter **31**, 285802 (2019).

[59] G. Acharya, B. Neupane, C.-H. Hsu, X. P. Yang, D. Graf, E. S. Choi, K. Pandey, M. R. U. Nabi, S. K. Chhetri, R. Basnet, S. Rahman, J. Wang, Z. Hu, B. Da, H. O. H. Churchill, G. Chang, M. Z. Hasan, Y. Wang, and J. Hu, Insulator-to-metal transition and isotropic gigantic magnetoresistance in layered magnetic semiconductors, Adv. Mater. **36**, 2410655 (2024).

[60] F. Holtzberg, T. R. McGuire, S. Methfessel, and J. C. Suits, Ferromagnetism in rare-earth group VA and VIA compounds with Th_3P_4 structure, J. Appl. Phys. **35**, 1033 (1964).

[61] R. C. Vickery and H. M. Muir, Anomalous thermoelectric properties of gadolinium selenide, Nature (London) **190**, 336 (1961).

[62] A. Kikkawa, K. Katsumata, S. Ebisu, and S. Nagata, Phase transition of a frustrated magnet α-Gd_2S_3, J. Phys. Soc. Jpn. **73**, 2955 (2004).

[63] L. M. Schoop, A. Topp, J. Lippmann, F. Orlandi, L. Müchler, M. G. Vergniory, Y. Sun, A. W. Rost, V. Duppel, M. Krivenkov, S. Sheoran, P. Manuel, A. Varykhalov, B. Yan, R. K. Kremer, C. R. Ast, and B. V. Lotsch, Tunable Weyl and Dirac states in the nonsymmorphic compound CeSbTe, Sci. Adv. **4**, eaar2317 (2018).

[64] K. Pandey, R. Basnet, A. Wegner, G. Acharya, M. R. U. Nabi, J. Liu, J. Wang, Y. K. Takahashi, B. Da, and J. Hu, Electronic and magnetic properties of the topological semimetal candidate NdSbTe, Phys. Rev. B **101**, 235161 (2020).

[65] C. C. Mayorga-Martinez, Z. Sofer, D. Sedmidubský, Š. Huber, A. Y. S. Eng, and M. Pumera, Layered metal thiophosphite materials: Magnetic, electrochemical, and electronic properties, ACS Appl. Mater. Interfaces **9**, 12563 (2017).

[66] R. Brec, Review on structural and chemical properties of transition metal phosphorous trisulfides MPS_3, Solid State Ion. **22**, 3 (1986).

[67] K. Okuda, K. Kurosawa, S. Saito, M. Honda, Z. Yu, and M. Date, Magnetic properties of layered compound $MnPS_3$, J. Phys. Soc. Jpn. **55**, 4456 (1986).

[68] R. Basnet, A. Wegner, K. Pandey, S. Storment, and J. Hu, Highly sensitive spin-flop transition in antiferromagnetic van der Waals material MPS_3(M = Ni and Mn), Phys. Rev. Mater. **5**, 064413 (2021).

[69] S. Gupta, K. G. Suresh, and A. K. Nigam, Magnetic, magnetocaloric and magnetotransport properties of $RSn_{1+x}Ge_{1-x}$ compounds (R = Gd, Tb, and Er; $x = 0.1$), J. Magn. Magn. Mater. **342**, 61 (2013).

[70] K. Pandey, D. Mondal, J. W. Villanova, J. Roll, R. Basnet, A. Wegner, G. Acharya, M. R. U. Nabi, B. Ghosh, J. Fujii, J. Wang, B. Da, A. Agarwal, I. Vobornik, A. Politano, S. Barraza-Lopez, and J. Hu, Magnetic topological semimetal phase with electronic correlation enhancement in SmSbTe, Adv. Quantum Technol. **4**, 2100063 (2021).

[71] G. Becker, J. Feldhaus, K. Westerholt, and S. Methfessel, Magnetic ordering and electrical conductivity in $La_{3-x}S_4$, $Gd_{3-x}S_4$ and $Ce_{3-x}S_4$, J. Magn. Magn. Mater. **6**, 14 (1977).

[72] M. Szlawska, D. Gnida, P. Ruszała, M. J. Winiarski, M. Samsel-Czekała, M. Schmidt, Y. Grin, and D. Kaczorowski, Antiferromagnetic ordering and transport anomalies in single-crystalline $CeAgAs_2$, Materials **13**, 3865 (2020).

[73] A. M. Goforth, P. Klavins, J. C. Fettinger, and S. M. Kauzlarich, Magnetic properties and negative colossal magnetoresistance of the rare earth zintl phase $EuIn_2As_2$, Inorg. Chem. **47**, 11048 (2008).

[74] J. Y. Chan, S. M. Kauzlarich, P. Klavins, R. N. Shelton, and D. J. Webb, Colossal negative magnetoresistance in an antiferromagnet, Phys. Rev. B **57**, R8103 (1998).

[75] C. Geibel Anupam and Z. Hossain, Magnetic behavior of $Eu_3Ni_4Ga_4$: Antiferromagnetic order and large magnetoresistance, J. Phys. Condens. Matter **24**, 326002 (2012).

[76] J.-S. Rhyee, B. K. Cho, and H.-C. Ri, Electrical transport properties and small polarons in $Eu_{1-x}Ca_xB_6$, Phys. Rev. B **67**, 125102 (2003).

[77] Z. L. Sun, A. F. Wang, H. M. Mu, H. H. Wang, Z. F. Wang, T. Wu, Z. Y. Wang, X. Y. Zhou, and X. H. Chen, Field-induced metal-to-insulator transition and colossal anisotropic magnetoresistance in a nearly Dirac material $EuMnSb_2$, npj Quantum Mater. **6**, 94 (2021).

[78] J. Seo, C. De, H. Ha, J. E. Lee, S. Park, J. Park, Y. Skourski, E. S. Choi, B. Kim, G. Y. Cho, H. W. Yeom, S.-W. Cheong, J. H. Kim, B.-J. Yang, K. Kim, and J. S. Kim, Colossal angular magnetoresistance in ferrimagnetic nodal-line semiconductors, Nature (London) **599**, 576 (2021).

[79] J. Kondo, Resistance minimum in dilute magnetic alloys, Prog. Theor. Phys. **32**, 37 (1964).

[80] G. Bergmann, Weak localization in thin films: a time-of-flight experiment with conduction electrons, Phys. Rep. **107**, 1 (1984).

[81] J. J. Lin and J. P. Bird, Recent experimental studies of electron dephasing in metal and semiconductor mesoscopic structures, J. Phys. Condens. Matter **14**, R501 (2002).

[82] D. T. Son and B. Z. Spivak, Chiral anomaly and classical negative magnetoresistance of Weyl metals, Phys. Rev. B **88**, 104412 (2013).

[83] A. A. Burkov, Chiral anomaly and transport in Weyl metals, J. Phys. Condens. Matter **27**, 113201 (2015).

[84] J. Xiong, S. K. Kushwaha, T. Liang, J. W. Krizan, M. Hirschberger, W. Wang, R. J. Cava, and N. P. Ong, Evidence for the chiral anomaly in the Dirac semimetal Na_3Bi, Science **350**, 413 (2015).

[85] Q. Li, D. E. Kharzeev, C. Zhang, Y. Huang, I. Pletikosić, A. V. Fedorov, R. D. Zhong, J. A. Schneeloch, G. D. Gu, and T. Valla, Chiral magnetic effect in $ZrTe_5$, Nat. Phys. **12**, 550 (2016).

[86] S. Y. Yu, Z. H. Liu, G. D. Liu, J. L. Chen, Z. X. Cao, G. H. Wu, B. Zhang, and X. X. Zhang, Large magnetoresistance in single-crystalline $Ni_{50}Mn_{50-x}In_x$ alloys ($x = 14-16$) upon martensitic transformation, Appl. Phys. Lett. **89**, 162503 (2006).

[87] B.A. Jones, The Kondo Effect, in *Handbook of Magnetism and Advanced Magnetic Materials: Fundamentals and Theory*, Vol. 1, edited by H. Kronmüller, S. Parkin, M. Fähnle, S. Maekawa, and I. Zutic (Wiley, 2007), pp. 149–163.

[88] P. Kumar, A. Dogra, P. P. S. Bhadauria, A. Gupta, K. K. Maurya, and R. C. Budhani, Enhanced spin–orbit coupling and charge carrier density suppression in $LaAl_{1-x}Cr_xO_3/SrTiO_3$ heterointerfaces, J. Phys. Condens. Matter **27**, 125007 (2015).

[89] H. Xue, Y. Hong, C. Li, J. Meng, Y. Li, K. Liu, M. Liu, W. Jiang, Z. Zhang, L. He, R. Dou, C. Xiong, and J. Nie, Large negative magnetoresistance driven by enhanced weak localization and Kondo effect at the interface of $LaAlO_3$ and Fe-doped $SrTiO_3$, Phys. Rev. B **98**, 085305 (2018).

[90] S. Barua, M. C. Hatnean, M. R. Lees, and G. Balakrishnan, Signatures of the Kondo effect in VSe_2, Sci. Rep. **7**, 1 (2017).

[91] I. Kar, S. Routh, S. Ghorai, S. Purwar, and S. Thirupathaiah, Observation of weak kondo effect and angle dependent magnetoresistance in layered antiferromagnetic V_5S_8 single crystal, Solid State Commun. **369**, 115209 (2023).